



LAWRENCE  
LIVERMORE  
NATIONAL  
LABORATORY

# Dynamic Changes in LSM Nanoparticles on YSZ: A Model System for Non-stationary SOFC Cathode Behavior

L. Y. Woo, R. S. Glass, R. J. Gorte, C. A. Orme,  
A. J. Nelson

January 7, 2009

Journal of The Electrochemical Society

## **Disclaimer**

---

This document was prepared as an account of work sponsored by an agency of the United States government. Neither the United States government nor Lawrence Livermore National Security, LLC, nor any of their employees makes any warranty, expressed or implied, or assumes any legal liability or responsibility for the accuracy, completeness, or usefulness of any information, apparatus, product, or process disclosed, or represents that its use would not infringe privately owned rights. Reference herein to any specific commercial product, process, or service by trade name, trademark, manufacturer, or otherwise does not necessarily constitute or imply its endorsement, recommendation, or favoring by the United States government or Lawrence Livermore National Security, LLC. The views and opinions of authors expressed herein do not necessarily state or reflect those of the United States government or Lawrence Livermore National Security, LLC, and shall not be used for advertising or product endorsement purposes.

# Dynamic Changes in LSM Nanoparticles on YSZ: A Model System for Non-stationary SOFC Cathode Behavior

Leta Y. Woo<sup>a</sup>, Robert S. Glass<sup>a</sup>, Raymond J. Gorte<sup>b</sup>, Christine A. Orme<sup>a</sup>, and A. J. Nelson<sup>a</sup>

<sup>a</sup>*Lawrence Livermore National Laboratory, Livermore, California 94551, USA*

<sup>b</sup>*Department of Chemical and Biomolecular Engineering, University of Pennsylvania, Philadelphia, Pennsylvania 19104, USA*

## Abstract

The interaction between nanoparticles of strontium-doped lanthanum manganite (LSM) and single crystal yttria-stabilized zirconia (YSZ) was investigated using atomic force microscopy (AFM), x-ray photoelectron spectroscopy (XPS), and scanning electron microscopy (SEM)/energy-dispersive x-ray spectroscopy (EDX). Nanoparticles of LSM were deposited directly onto single crystal YSZ substrates (100) using an ultrasonic spray nozzle. As samples were annealed from 850°C to 1250°C, nanoparticles gradually decreased in height and eventually disappeared completely. Subsequent reduction in  $\text{H}_2/\text{H}_2\text{O}$  at 700°C resulted in the reappearance of nanoparticles. Studies were carried out on identical regions of the sample allowing the same nanoparticles to be characterized at different temperatures. Morphological changes indicate the formation of a thin layer of LSM, and XPS results support the observation by indicating an increase in signal from the La and Sr and a decrease in signal from the Y and Zr with increasing temperature. SEM/EDX was used to verify that the nanoparticles in the reduced sample contained La. The changes in the LSM/YSZ morphology may be important in explaining the non-stationary behavior observed in operating fuel cells. The thin layer of LSM initially results in poor cathode performance; reducing conditions then lead to film disruptions, indicating nano/microporosity, that increase oxygen ion diffusion and performance.

## Introduction

Compared with conventional methods of power generation (i.e., combustion of fossil fuels), solid-oxide fuel cells (SOFCs) could dramatically reduce greenhouse gases or be carbon neutral. The high efficiency of SOFCs results from the direct conversion of chemical to electrical energy at high temperatures, typically  $>600^{\circ}\text{C}$ . Compared with other types of fuel cells, fuel flexibility is a major advantage of SOFCs and allows the use of any combustible fuel (not just hydrogen), including biofuels.

Strontium-doped lanthanum manganite (LSM) has been used as the state-of-the-art cathode material in commercial SOFCs primarily due to its mechanical and thermodynamic stability. Mechanical stability results from the ability to match the thermal expansion of the electrolyte, yttria-stabilized zirconia (YSZ). LSM is also relatively more thermodynamically stable compared to other mixed conductors containing Co, which tend to form insulating zirconates at the high temperatures (greater than  $1200^{\circ}\text{C}$ ) typically necessary to process the composites. Nevertheless, the physics governing the LSM/YSZ interfacial behavior remain poorly understood.<sup>1</sup> In particular, cells using LSM/YSZ exhibit non-stationary activation/deactivation behavior during operation, where the measured performance depends on both processing and operational history. The non-stationary behavior complicates data comparison and evaluation. Understanding its behavior would also provide a framework for investigating related materials that have the

potential for better performance.

The initial performance of an operating SOFC with an LSM cathode can be poor; however, significant improvements can occur after the cell has been operated under polarization/biasing for a period of time, typically on the order of minutes to hours. The non-stationary activation behavior is hysteretic, and the non-activated state can be recovered by removing the polarization and leaving the cell at open circuit for a period of time, typically on the order of hours. Efforts to explain the activation phenomena have focused on mechanisms related to the partial reduction of LSM and include the reduction of  $\text{La}_2\text{Zr}_2\text{O}_7$  (an insulating phase) that may have formed at the LSM-YSZ interface,<sup>2,3</sup> the reduction of manganese oxide species that extend the triple phase boundary,<sup>4-6</sup> the removal of surface species that might otherwise passivate the interface,<sup>7</sup> the surface enrichment of La species that improves electrode performance by an unexplained mechanism,<sup>8</sup> and the formation of nanopores or other microstructural changes that improve oxygen diffusion to the interface.<sup>9-11</sup>

Investigation of microstructural changes in SOFCS cathodes typically involve postmortem destructive analysis of interfaces including sectioning and acid etching.<sup>7,9,11</sup> A non-destructive method for examining interfacial phenomena, both microstructural and chemical, should be expected to provide more fundamental insight into activation/deactivation processes. The benefit of using a model system to investigate dynamic phenomena has been

previously shown by Hansen et al.<sup>12</sup> In their work, changes in gaseous environment were found to cause reversible shape changes in supported copper nanocrystals used as hydrocarbon catalysts. In our work, a model system was investigated consisting of LSM nanoparticles deposited directly on a single crystal YSZ (100) substrate. Analysis of identical sample regions after annealing over a range of temperatures in ambient air and then after being subjected to a reducing atmosphere of  $\text{H}_2/\text{H}_2\text{O}$  was performed to investigate changes at the LSM/YSZ interface.

## Experimental

Commercial (Praxair) nominal  $(\text{La}_{0.85}\text{Sr}_{0.15})_{0.98}\text{Mn}$  Oxide (LSM) powder with particle size of  $d_{50}=0.9\text{ }\mu\text{m}$  and surface area of  $8.7\text{ m}^2/\text{g}$  was ball-milled in a 50/50 by volume solution of water and ethanol overnight. The water/ethanol mixture with LSM powder was then allowed to settle, and the fine particle slurry from the top of the mixture was extracted to use for deposition. An ultrasonic spray nozzle was used to deposit the slurry onto  $10\text{ mm} \times 10\text{ mm} \times 0.5\text{ mm}$  single crystal yttria-stabilized zirconia (100) substrates (MTI Corporation). During deposition, the substrates were heated to  $120^\circ\text{C}$  to evaporate the solvent. Samples were subsequently annealed for four hours at 850, 1050, 1150, and  $1250^\circ\text{C}$ , using ramp-up and cool-down rates of  $2^\circ\text{C}/\text{min}$ . The anneal rates and times were assumed to be sufficient for reaching equilibrium, and studying the effect of ramp/cool rates and/or

anneal times were outside the scope of the current work. After the final anneal temperature at 1250°C, samples were also reduced overnight in wet ( $\sim 3\%$   $\text{H}_2\text{O}$ )  $\text{H}_2$  at 700°C.

The morphology and topology of the LSM nanoparticles deposited onto the single crystal YSZ substrate were investigated using tapping-mode atomic force microscopy (AFM). The examination was done under ambient conditions on a commercial Digital Instruments NanoScope Dimension IIIA microscope and used n-doped silicon probes with a tip radius between 10 and 15 nm.  $10\ \mu\text{m} \times 10\ \mu\text{m}$  fiducial marks were placed on the sample using a nanoindenter to allow identical regions to be characterized with the AFM and compared after heat treatment. AFM images were taken at least  $500\ \mu\text{m}$  away from the nanoindentations. Image SXM software was used for particle analysis.

Surface composition was investigated using x-ray photoelectron spectroscopy (XPS) analysis, which was performed on a PHI Quantum 2000 system using a focused monochromatic Al  $\text{K}\pm$  x-ray (1486.7 eV) source for excitation and a spherical sector analyzer. The instrument has a 16-element multichannel detection system. A  $200\ \mu\text{m}$  diameter x-ray beam was used for analysis. The x-ray beam is incident normal to the sample and the x-ray detector is at  $45^\circ$  away from the normal. The pass energy was 23.5 eV giving an energy resolution of 0.3 eV that when combined with the 0.85 eV full width at half maximum (FWHM) Al  $\text{K}\pm$  line width gives a resolvable



XPS peak width of 1.2 eV FWHM. Deconvolution of non-resolved peaks was accomplished using Multipak 6.1A (PHI) curve fitting routines. The collected data were referenced to an energy scale with binding energies for Cu 2p<sub>3/2</sub> at  $932.72 \pm 0.05$  eV and Au 4f<sub>7/2</sub> at  $84.01 \pm 0.05$  eV. Binding energies were also referenced to the C 1s photoelectron line arising from adventitious carbon at 284.8 eV. Low energy electrons were used for specimen neutralization. Scanning electron microscopy (SEM) with energy dispersive x-ray analysis (EDX) were used to investigate the bulk composition of individual nanoparticles.

## Results

Figure 1 shows an AFM amplitude image ( $25 \mu\text{m} \times 25 \mu\text{m}$  scan) of LSM nanoparticles deposited onto single crystal YSZ (100) annealed at 850°C. As indicated in Fig. 1, two areas with different particle densities (labeled region I and II) were examined in more detail using  $3 \mu\text{m} \times 3 \mu\text{m}$  scans and will be discussed below. Additional regions were also investigated and demonstrated similar-type behavior. A range of particle sizes and distributions were deposited onto the substrate.

Figures 2 and 3 show  $3 \mu\text{m} \times 3 \mu\text{m}$  amplitude scans of regions I and II, respectively, at the four different annealing temperatures. LSM particle sizes range from approximately 20 to 300 nm in diameter. As annealing temperature increased from 850°C to 1250°C, smaller particles present at 850°C

disappeared first, followed by larger particles. All the particles disappeared at the highest annealing temperature of 1250°C.

Whereas particles seem to disappear as the anneal temperature increases in region I, region II indicates smaller particles coalescing into larger particles and the appearance of a terraced or stepped morphology at 1050°C, as shown in Fig. 3(b). The most notable difference between the two regions is that region II has almost three times the particle density of region I, with 89 particles/ $\mu\text{m}^2$  compared to 36 particles/ $\mu\text{m}^2$ . Furthermore in Fig. 3(c), at 1150°C, film formation in the high-density region (region II) is indicated by perturbations around the larger particles, which seem to be disrupting the film growth. Closer examination of the low-density region (region I) at 1150°C (Fig. 2(c)) also indicates similar-type behavior with larger particles disturbing film growth.

The observation that smaller particles coalesce into larger particles in the high-density region along with the appearance of stepped/terraced morphology seems to imply that particles are diffusing along the surface of the substrate and are not diffusing directly into the substrate. Additional analysis, discussed below, supports the formation of a thin film or coating with increasing temperature.

To illustrate the changes in particle morphology, Fig. 4(a) shows the AFM topography image ( $3\ \mu\text{m} \times 3\ \mu\text{m}$  scan) of the low-density region and indicates two line sections used for the height profiles shown in Figs. 4(b)

and (c). The small particles ( $\sim 40$  nm in diameter,  $\sim 3$  to 5 nm in height) in Fig. 4(b) were initially present at  $850^\circ\text{C}$ , but then disappear at  $1050^\circ\text{C}$ . The large particles ( $\sim 200$  to 300 nm in diameter,  $\sim 60$  to 100 nm in height) in Fig. 4(c) do not disappear and decrease in height as annealing temperature increases. Figure 5 shows height profiles taken from the high-density region and indicates more dramatic decreases in initial particle height at  $1050^\circ\text{C}$  compared to similarly sized particles in the low-density region and will be discussed in more detail below.

The initial particle morphologies at  $850^\circ\text{C}$  typically consisted of single rounded peaks. For particles that persist at  $1050^\circ\text{C}$ , in addition to height reduction, changes in morphology included the appearance of multiple rounded peaks replacing the single rounded peak. The height profiles for particles in both the low- and high-density regions (Figs. 4(c) and 5) show that particle diameter remained relatively unchanged at  $1050^\circ\text{C}$ , and that the particle volume is decreasing along with the height. Furthermore, the volume continues to decrease at  $1150^\circ\text{C}$  forming flat structures only a few nanometers (1 to 3 nm) in height, while the diameter of the particles decreased by approximately 100 and 50 nm in the low- and high-density regions, respectively.

Particle volumes were calculated by approximating the geometry as a spherical cap and using the radius and height of each particle, which were determined using the particle analysis tool in the Image SXM software. The

volume of a spherical cap is given by the following equation:

$$V = \frac{\pi h(3a^2 + h^2)}{6} \quad (1)$$

where  $h$  is the height and  $a$  is the radius.

The particle volume distribution at 850°C in low-density regions is shown in Fig. 6, where 74% of the particles had volumes of less than  $2 \times 10^{-6} \mu\text{m}^3$ . Figure 7 shows the change in particle volume at 1050°C as a function of the initial particle volume at 850°C. The dotted line represents the relationship for particles that disappear at 1050°C, or when the particle volume at 850°C equals the change in particle volume at 1050°C. In Fig. 7, particles with volumes less than approximately  $3 \times 10^{-4} \mu\text{m}^3$  disappear at 1050°C, and correspond with the dotted line. The inset of Fig. 7 shows in more detail the behavior of particles with volumes less than  $10 \times 10^{-6} \mu\text{m}^3$ , which all disappear at 1050°C and correspond with the dotted line.

At 850°C, as particle volume increases, the data begin to deviate from the dotted line behavior revealing that larger particles continue to decrease in volume, but no longer disappear at 1050°C. Comparing the data in Fig. 7 with the particle volume distribution in Fig. 6 indicates that only a small number (about 6%) of the original particles remain in the low-density regions at 1050°C. Furthermore, Fig. 7 also shows two data points (open squares) from the high-density region for particles with similar volumes as those in the low-density region. The data from the high-density region demonstrate a much more dramatic decrease in volume, as indicated previously in Fig. 5

by the height profile.

The changes in particle volume at 1050°C indicate that above a threshold value for volume (about  $3 \times 10^{-4} \mu\text{m}^3$ ), the particles no longer disappear. Furthermore, the limited data for the particles that persist at 1050°C reveal a slight dependence of the volume change on the initial particle volume. Larger initial particle volumes at 850°C have larger volume changes at 1050°C. The trend seems to suggest that in the low-density region, the surface concentration or volume of each particle is dominating the diffusion behavior.

AFM tip convolution was considered when evaluating structures with heights less than the tip radius dimension (10 to 15 nm), as was the case for the flat structures of only a few nanometers in height. The tip radius dimension is approximated by considering the very end of the tip to be spherically shaped with radius  $R$ . Figure 8 shows a schematic diagram of AFM tip convolution where  $R$  is the radius of the tip,  $h$  is the step height, and  $w$  is the measured width.<sup>13</sup> The relationship between the parameters can then be estimated using the following equation:

$$R = \frac{h^2 + w^2}{2h} \quad (2)$$

For particles with heights ranging from 1 to 3 nm that are imaged using a tip radius ranging from 10 to 15 nm, measured widths range from 4 to 9 nm. Since particle diameters were all greater than 40 nm, the additional convolution in the measured width should not significantly alter the analysis.

To further investigate the behavior of the LSM nanoparticles on the single crystal YSZ (100) substrate, the same sample that was heated to 1250°C was then treated in a reducing atmosphere ( $\text{H}_2/\text{H}_2\text{O}$ ) at 700°C. Figures 9a and b show  $3\text{ }\mu\text{m} \times 3\text{ }\mu\text{m}$  scans of the low-density (region I) and high-density (region II) regions, respectively, after reduction at 700°C, and clearly demonstrate the reappearance of spherical nanoparticles. The additional surface roughness was due to depositing sputtered carbon, which was necessary to perform scanning electron microscopy (SEM) with energy dispersive x-ray spectroscopy (EDX) analysis of the same samples. Nevertheless, the nanoparticles that reappear do not have any spatial relationships to the original deposited nanoparticles (see Figs. 2 and 3), and further supports the observation from AFM measurements of film formation. If the nanoparticles were disappearing by diffusing into the substrate, the nanoparticles that reappeared would likely be correlated with their original positions. Figure 9c shows height profiles for line sections in the reduced sample indicating particle sizes ranging from approximately 100 to 150 nm in diameter and 20 to 60 nm in height. Also, the nanoparticles that reappeared exhibit two different peak morphologies. There is evidence for a single rounded peak, similar to particles that were initially deposited and annealed at 850°C. The other particles in Fig. 9 exhibit a flattened peak.

To investigate the composition of the nanoparticles that reappear on the reduced sample, scanning electron microscopy (SEM) with energy disper-

sive x-ray spectroscopy (EDX) was employed. Due to the large background signal from the YSZ substrate relative to the small amount of LSM nanoparticles, only the La peaks were discernible in the EDX spectra. Although the results for the  $3\text{ }\mu\text{m} \times 3\text{ }\mu\text{m}$  regions discussed previously indicate film formation at  $1250^{\circ}\text{C}$ , with no evidence of individual LSM nanoparticles, other regions of the sample did contain evidence of LSM particles and were used for SEM/EDX analysis. Similar spectra were obtained with spot EDX analysis of the LSM nanoparticles in samples annealed at  $850$ ,  $1150$ , and  $1250^{\circ}\text{C}$  as the nanoparticles that reappeared after reducing the sample in wet  $\text{H}_2$  at  $700^{\circ}\text{C}$ . The spot EDX results indicate that the nanoparticles that reappear after reduction contain La and appear to be similar to the original nanoparticles that were deposited.

X-ray photoelectron spectroscopy (XPS) analysis was used to examine the surface composition of LSM nanoparticles deposited on single crystal YSZ (100) after annealing to  $1150^{\circ}\text{C}$  and  $1250^{\circ}\text{C}$ . The XPS analysis used a  $200\text{ }\mu\text{m}$  diameter x-ray beam and was performed on the same samples used for the AFM analysis. The atomic concentrations are summarized in table 1.

Table 1 shows that the XPS analysis did not resolve contributions from Mn on the surface at  $1150^{\circ}\text{C}$  and  $1250^{\circ}\text{C}$ , which is discussed in more detail below. Both the Sr:O and La:O ratios increase with temperature from 0.008 at  $1150^{\circ}\text{C}$ , to 0.015 and 0.009, respectively, at  $1250^{\circ}\text{C}$ . For comparison,

both the Y:O and Zr:O ratios decrease with temperature from 0.11 and 0.32, respectively, at 1150°C, to 0.09 and 0.28, respectively, at 1250°C. Also, both the Sr and La signals increase relative to the Y and Zr signals, as shown in Fig. 10. The relative increases in the Sr and La signals in combination with the relative decreases in the Y and Zr signals seem to indicate that the LSM nanoparticles are spreading out over the surface of the single crystal YSZ.

Figure 11 compares the XPS survey spectra for the LSM powder used for deposition and a separate sample (not the same sample used for AFM analysis) with LSM nanoparticles deposited on single crystal YSZ (100) annealed at 850°C. The sample annealed at 850°C had a higher particle loading than the sample used for both AFM and XPS analysis at 1150°C and 1250°C (the data shown in Fig. 10). In Fig. 11, the contributions from La, Mn, and Sr are clearly evident for the LSM powder. However, only contributions from La and Sr are discernible in the survey spectra for the LSM/YSZ sample annealed at 850°C. Considering the relative peak intensities between La3d and Mn2p in the LSM powder, the amount of decrease in the La3d peak in the 850°C LSM/YSZ sample would lead to a relative Mn2p intensity too small to be resolved. Therefore, the absence of the Mn peak at 850°C (as well as at the higher temperatures) could be due to lack of resolution and not necessarily changes in Mn surface concentration.

Since the sample annealed at 850°C had a higher particle loading than the 1150/1250°C sample, the signals relative to O, Zr, and Y cannot be com-



pared directly. Nevertheless, the Sr:La ratio can be reasonably compared for the different samples and is shown to increase with increasing temperature. The Sr:La ratio for the powder sample as measured by the XPS analysis was 0.23, which is in reasonable agreement with the calculated value of 0.18 for 15% Sr doping. For the sample annealed at 850°C, the Sr:La increased to 0.40, with further increases to 0.99 and 1.15 as the anneal temperature increased to 1150°C and 1250°C, respectively. The increasing Sr:La ratio could be indicating Sr segregation to the surface as temperature increases, and has been previously reported.<sup>7,14–16</sup>

## Discussion

The decrease in LSM nanoparticle height with increasing temperature and the formation of a film at temperatures above 1050°C is in agreement with previously published work.<sup>17</sup> The previous work by Huang et al. used a spray-deposited dilute aqueous solution of La, Sr, and Mn salts that was subsequently calcined in air to form the perovskite phase. Their AFM measurements also show non-uniform particle distribution, with a mixture of mostly irregularly-shaped particles, but also some rectangular-shaped particles that were approximately 30 nm in height at 850°C. Huang et al. attempted to examine similar areas of the sample at different temperatures, and representative particles were shown to grow in diameter, without changing height, and adopt a more pronounced rectangular shape after heating

to 1050°C. Further heating to 1150°C resulted in representative particles with even larger diameters and reduced heights of about 5 nm. Huang et al. suggest that the rectangular-shaped particles indicate epitaxy between the LSM and YSZ and imply strong interactions between the oxides.

Unlike the previous work by Huang et al., our study uses identical regions of the same sample to investigate the effect of different annealing temperatures. Also, we deposited LSM nanoparticles of a known composition directly on the single crystal YSZ (100) substrate instead of decomposing and calcining the LSM from an aqueous salt solution. Furthermore, we did not find overwhelming evidence of oriented or rectangular-shaped particles in the regions investigated. The rectangular-shaped particles seen in previous work could be due to an effect associated with forming the perovskite phase from the dilute salt solution instead of directly depositing the nanoparticles. Nevertheless, our results confirm previous findings where LSM exhibits wetting phenomena on the YSZ and strong oxide-oxide interaction, and although rectangular-shaped morphology was not evident, the evolution of the film growth with steps and terraces could possibly be due to an epitaxial growth mechanism.

Our results reinforce that the introduction of nano/microporosity within the LSM is responsible for the non-stationary activation/deactivation behavior in LSM/YSZ composites. After processing at temperatures above 1050°C, LSM particles form a dense film on YSZ that limits the diffusion of

oxygen ions to the triple-phase boundary (TPB). At lower temperatures of 700°C, reducing conditions created by flowing  $\text{H}_2/\text{H}_2\text{O}$  result in disruptions of the dense LSM film (as indicated by the reappearance of nanoparticles in our work), which may then introduce nano/microporosity that allow easier oxygen ion diffusion to the TPB. Previous work strengthens this argument by confirming the formation of a dense LSM film by using Brunauer-Emmett-Teller (BET) surface area measurements in LSM/YSZ composite cathodes calcined above 1050°C that then exhibited activation/deactivation.<sup>10</sup> In that same work, samples annealed at lower temperatures, 850°C, did not form a thin LSM coating nor exhibit non-stationary behavior. The correlation between the temperature at which a thin LSM coating forms and the advent of non-stationary activation/deactivation behavior implicates nano/microporosity within the LSM as an explanation for the behavior.

To further elucidate the LSM wetting/dewetting mechanism responsible for generating nano/microporosity, our work provides insight on the mobility of LSM on YSZ by characterizing identical regions and nanoparticles at different temperatures. Figure 12(a) shows a schematic of the LSM particle on the YSZ substrate indicating the possible pathways for particle dissolution. Our results support a surface diffusion mechanism.

Also, the two regions studied in detail seem to exhibit differing rates of LSM mobility, with more dramatic decreases in height in the low-density region (region I) compared to the high-density region (region II) for similarly

shaped/sized particles at 1050°C. Figure 12(b) and (c) show schematics of the paths available on the low- and high-density regions, respectively. A notable difference between the two regions was the appearance of steps and terraces in the film morphology of the high-density region, which did not appear in the low-density region, at 1050°C (see Figs. 2b and 3b). A possible explanation for the differing mobilities in the two regions is the effect of linear defects, for example steps or terraces, to induce a strong diffusion anisotropy.<sup>18-22</sup> Enhanced diffusion has been shown to occur along step edges and have been associated with differences in binding energies and diffusion activation energies along the step edge compared to on the terrace.<sup>22</sup> The higher particle density in region II leads to the formation of surface steps and terraces at 1050°C that would then also increase diffusion rates for larger particles. The effect is not seen in region I due to the lower particle density and different surface morphology at 1050°C.

At 1150°C, the particle mobility in the two regions shows the opposite trend of the behavior seen previously at 1050°C. At 1150°C, changes in particle volume in the low-density region indicate faster mobility (at 1050°C, the mobility was slower) than the high-density region. After annealing to 1150°C, particles continue to decrease in height in the low-density region, but in the high-density region, the particle heights remain constant with only a slight decrease in diameter. Again, particle density could be playing a role. At 1150°C, due to the changing morphology, linear defects no longer control

the diffusion behavior in the high-density region, and the effect of higher coverage may begin to dominate and actually inhibit surface diffusion. In the low-density region, the lower surface coverage allows the concentration gradient to continue to drive the diffusion process responsible for reducing the particle height. The differing particle mobility in the two regions at 1050°C and 1150°C indicates complex behavior that could be influenced by morphology, coverage, and possibly other competing phenomena. Nevertheless, over the temperature range, LSM is mobile on the YSZ, and despite the varying particle densities and non-uniform particle dimensions (both height and diameter), there is evidence of a strong driving force for the LSM to coat the YSZ substrate as temperature increases.

LSM surface mobility on YSZ is clearly demonstrated in our work and the driving force for LSM wetting the substrate could be attributed to reductions in surface and interface energies. The YSZ substrate has a cubic fluorite structure that consists of alternating rows of cations ( $\text{Zr}^{4+}$ ) and anions ( $\text{O}^{2-}$ ) along the [100] direction. Therefore, the (100) plane can have two different atomically flat terminations with different structures and stoichiometries, but both of which are polar, and therefore have higher surface energies.<sup>23,24</sup> The interface energy between YSZ and LSM is likely to be low due to film-substrate bonding owing to some chemical reactivity between the LSM and YSZ and the similarity in ionic bonding within the two materials. Also, LSM may be able to provide a polar surface of opposite charge to the polar

YSZ surface causing further decreases in interface energy. Therefore, the driving force for LSM spreading on the YSZ as temperature increases could reasonably be explained by the decrease in the YSZ polar surface, which has high surface energy, with increases in the LSM/YSZ interface, which has lower energy.

The reappearance of nanoparticles after reduction should also be considered in terms of changes in surface and interface energies. Recent work by Zhang et al. postulates that at lower oxygen pressures, YSZ becomes oxygen deficient and generates vacancies that allow the (100) surface to relax and lower the surface energy.<sup>24</sup> They support their assertion by citing several previous works that relate changes in charge distribution on surfaces with surface relaxation. The surface relaxation behavior was used to explain their observation that (001)-oriented YSZ films were grown during pulsed laser deposition at low oxygen pressures. The lower YSZ surface energy during reduction could serve as a driving force to disrupt the LSM coating.

The reappearance of nanoparticles may also be related to changes in the LSM/YSZ interface energy during reduction. LSM has a perovskite-type structure and exhibits variable oxygen non-stoichiometry. The extent of non-stoichiometry depends on the doping level of Sr, temperature, and partial pressure of oxygen.<sup>1,25-27</sup> Furthermore, previous work has demonstrated that the LSM lattice parameter also changes with oxygen stoichiometry.<sup>27</sup>

The typical lattice parameter for the commercial YSZ single crystal sub-

strate used in our study was reported as 5.125Å. The calculated lattice mismatch between the YSZ and LSM would be about 7-8% based on reports for LSM with Sr doping levels of around 0.15.<sup>26,27</sup> Previous work has demonstrated that LSM films can grow with the in-plane epitaxial variant structure on single crystal substrates of  $\text{ZrO}_2(\text{Y}_2\text{O}_3)$  with (001) orientation.<sup>28</sup> LSM has a larger lattice parameter than YSZ, and the lattice parameter has been shown to increase linearly with decreasing oxygen content.<sup>27</sup> The unit cell expansion seems consistent with increases in oxygen vacancies (and increases in electrons) compensated by decreases in the Mn oxidation state. The decreased Mn oxidation state produces Mn ions with a larger ionic radius. The increasing lattice parameters could also be related to the displacement of atoms in the perovskite lattice resulting from the formation of oxygen vacancies where the metal atoms relax away from the vacant site while the oxygen atoms relax toward the vacant site. Increases in lattice parameters with decreasing oxygen concentration have been seen in other types of perovskites.<sup>29</sup>

The increasing LSM lattice parameter under reducing conditions and resulting increases in lattice mismatch with the YSZ could be a factor in increasing the interface energy. The increased interface energy, along with the possible decrease in YSZ surface energy discussed above, would then no longer favor the LSM spreading over the YSZ and result in the reappearance of nanoparticles.

## Conclusions

Our results using a model system support a mechanism responsible for the non-stationary behavior of LSM/YSZ related to the initial formation of a dense layer of LSM that inhibits oxygen ion diffusion to the TPB. Reducing conditions, which are analogous to cathodic polarization, then disrupt the dense layer and create nanoporosity that increases oxygen ion diffusion to the TPB. The model system, consisting of LSM nanoparticles deposited on YSZ single crystal substrates (100), clearly showed LSM nanoparticle mobility at 1050°C and 1150°C followed by the formation of a film at 1250°C. Subsequent annealing at 700°C in a reducing mixture of H<sub>2</sub>/H<sub>2</sub>O resulted in the reappearance of nanoparticles.

## Acknowledgements

This work was performed under the auspices of the U.S. Department of Energy by Lawrence Livermore National Laboratory under Contract DE-AC52-07NA27344. Support was provided by the U.S. Department of Energy's Hydrogen Fuel Initiative (grant DE-FG02-05ER15721).



## References

1. S. B. Adler, *Chem. Rev.*, **104**, 4791 (2004).
2. A. Mitterdorfer and L. J. Gauckler, *Solid State Ionics*, **111**, 185 (1998).
3. H. Yokokawa, *Annu. Rev. Mater. Res.*, **33**, 581 (2003).
4. X. J. Chen, S. H. Chan, and K. A. Khor, *Solid State Ionics*, **164**, 17 (2003).
5. M. Backhaus-Ricoult *Solid State Ionics*, **177**, 2195 (2006).
6. M. Backhaus-Ricoult, K. Adib, T. St. Clair, B. Luerssen, L. Gregoratti, and A. Barinov, *Solid State Ionics*, **179**, 891 (2008).
7. S. P. Jiang, *J. Solid State Electrochem.*, **11**, 93 (2007).
8. A. A. Vance and S. McIntosh, *J. Electrochem. Soc.*, **155**, B1 (2008).
9. M. Kuznecov, P. Otschik, P. Obenaus, K. Eichler, and W. Schaffrath, *Solid State Ionics*, **157**, 371 (2003).
10. Y. Y. Huang, J. M. Vohs, and R. J. Gorte, *J. Electrochem. Soc.*, **152**, A1347 (2005).
11. X. J. Chen, K. A. Khor, and S. H. Chan, *J. Power Sources*, **123**, 17 (2003).

12. P. L. Hansen, J. B. Wagner, S. Helveg, J. R. Rostrup-Nielsen, B. S. Clausen, and H. Topsøe, *Science*, **295**, 2053 (2002).
13. S. Xu, N. A. Amro, and G.-Y. Liu, *Appl. Surf. Sci.*, **175-176**, 649 (2001).
14. Q. -H. Wu, M. Liu, and W. Jaegermann, *Mater. Lett.*, **59**, 1480 (2005).
15. S. Fearn, J. Rossiny, and J. Kilner, *Solid State Ionics*, **179**, 811 (2008).
16. T. T. Fister, D. D. Fong, J. A. Eastman, P. M. Baldo, M. J. Highland, P. H. Fuoss, K. R. Balasubramaniam, J. C. Meador, and P. A. Salvador, *Appl. Phys. Lett.*, **93**, 151904 (2008).
17. Y. Huang, J. M. Vohs, and R. J. Gorte, *Electrochem. Solid-State Lett.* , **9**, A237 (2006).
18. A. G. Naumovets and Z. Zhang, *Surf. Sci.*, **500**, 414 (2002).
19. H. Wagner, in *Surface Mobilities on Solid Materials*, V. T. Binh, Editor, p. 161, Plenum Press, New York (1983).
20. C. Uebing and R. Gomer, *Surf. Sci.*, **317**, 165 (1994).
21. J. Ma, X. Xiao, and M. M. T. Loy, *Surf. Sci.*, **436**, L661 (1999).
22. A. Natori and R. W. Godby, *Phys. Rev. B*, **47**, 15816 (1993).
23. O. Maksimov, P. Fisher, M. Skowronski, P. A. Salvador, M. Snyder, J. Xu, and X. Weng, *J. Cryst. Growth*, **310**, 2760 (2008).

- 24. X. Zhang, B. Berdahl, A. Klini, C. Fotakis, and S. S. Mao, *Appl. Phys. A*, **91**, 407 (2008).
- 25. J. H. Kuo, H. U. Anderson, and D. M. Sparlin, *J. Solid State Chem.*, **83**, 52 (1989).
- 26. R. Millini, M. F. Gagliardi, and G. Piro, *J. Mater. Sci.*, **29**, 4065 (1994).
- 27. Z. Bukowski, B. Dabrowski, J. Mais, P. W. Klamut, S. Kolesnik, and O. Chmaissem, *J. Appl. Phys.*, **87**, 5031 (2000).
- 28. O. Yu. Gorbenko, A. R. Kaul, A. A. Kamenev, O. V. Melnikov, I. E. Graboy, N. A. Babushkina, A. N. Taldenkov, and A. V. Inyuskin, *J. Cryst. Growth*, **275**, e2453 (2005).
- 29. C. Wang, B. L. Cheng, S. Y. Wang, H. B. Lu, Y. L. Zhou, Z. H. Chen, and G. Z. Yang, *Thin Solid Films*, **485**, 82 (2005).

## List of Figures

Fig. 1: AFM amplitude image ( $25\ \mu\text{m} \times 25\ \mu\text{m}$  scan) of LSM nanoparticles deposited onto single crystal YSZ (100) annealed at  $850^\circ\text{C}$  indicating two areas, labeled I and II, that were examined in more detail using  $3\ \mu\text{m} \times 3\ \mu\text{m}$  scans.

Fig. 2: AFM amplitude images ( $3\ \mu\text{m} \times 3\ \mu\text{m}$  scans) of region I (see Fig. 1) with a relatively low particle density of  $36\ \text{particles}/\mu\text{m}^2$  annealed at different temperatures.

Fig. 3: AFM amplitude images ( $3\ \mu\text{m} \times 3\ \mu\text{m}$  scans) of region II (see Fig. 1) with a relatively high particle density of  $89\ \text{particles}/\mu\text{m}^2$  annealed at different temperatures.

Fig. 4: (a) AFM topography image ( $3\ \mu\text{m} \times 3\ \mu\text{m}$  scan) indicating the height profiles for two line sections, (b) and (c), in the low-density region at different temperatures. Particle height decreases as annealing temperature increases.

Fig. 5: Height profile from the line section indicated in the AFM topography image ( $3\ \mu\text{m} \times 3\ \mu\text{m}$  scan, shown in the inset) of the high-density region. Particle height decreases as annealing temperature increases.

Fig. 6: The distribution of particle volumes at  $850^\circ\text{C}$  in the low-density regions.

Fig. 7: The change in particle volume at  $1050^\circ\text{C}$  as a function of the initial particle volume at  $850^\circ\text{C}$ . The dotted line represents the relationship for

particles that disappear at 1050°C, or when the particle volume at 850°C equals the change in particle volume at 1050°C.

Fig. 8: Schematic diagram of AFM tip convolution where  $R$  is the radius of the tip,  $h$  is the step height, and  $w$  is the measured width.<sup>13</sup>

Fig. 9: AFM amplitude images ( $3\ \mu\text{m} \times 3\ \mu\text{m}$  scans) of the sample reduced at 700°C in  $\text{H}_2/\text{H}_2\text{O}$  for (a) low-density region I and (b) high-density region II. (c) Height profiles, as indicated by the line sections in the inset AFM topography scans ( $3\ \mu\text{m} \times 3\ \mu\text{m}$ ). The additional surface roughness is due to sputtered carbon deposition used for SEM/EDX analysis.

Fig. 10: From the atomic concentrations in table 1 calculated from the XPS analysis, both the Sr and La signals increase relative to the Y and Zr signals as the annealing temperature increased from 1150°C to 1250°C and indicates that the LSM nanoparticles are spreading out over the surface of the single crystal YSZ.

Fig. 11: The XPS survey spectra for LSM powder by itself and LSM nanoparticles deposited on single crystal YSZ (100) annealed at 850°C.

Fig. 12: Schematic of (a) possible pathways for particle dissolution, (b) available surface pathway in the low-density region, and (c) additional pathway in the high-density region along the terrace/step edge which may enhance diffusion.

Table 1: Surface composition, determined using XPS, of LSM nanoparticles deposited on single crystal YSZ (100) after annealing at 1150°C and 1250°C.

	atom concentration (at. %)					
	La	Sr	Mn	O	Y	Zr
1150°C	0.53	0.57	0	68.99	7.60	22.31
1250°C	0.67	1.09	0.01	71.84	6.35	20.05

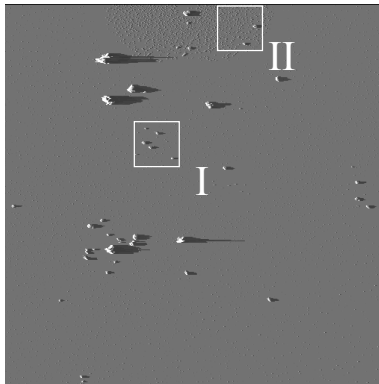


Figure 1:

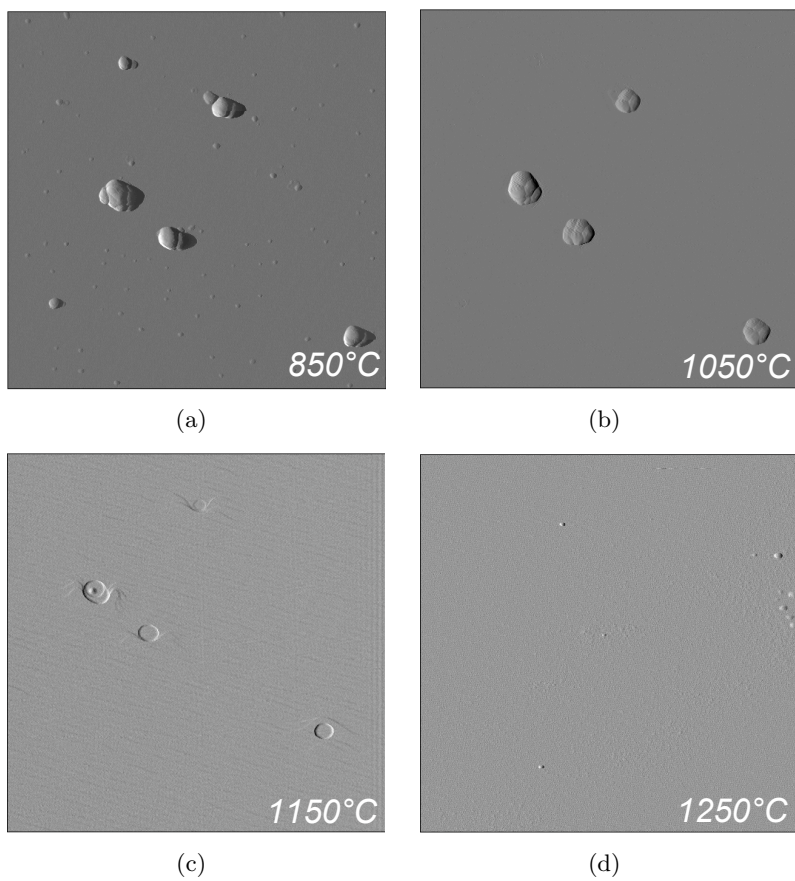


Figure 2:



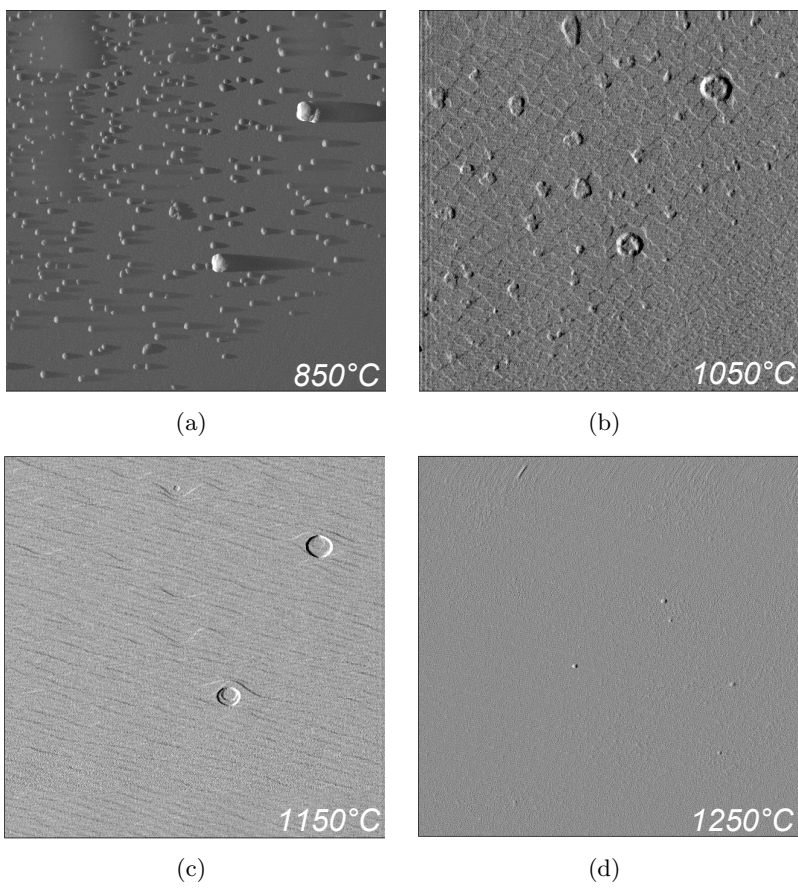


Figure 3:

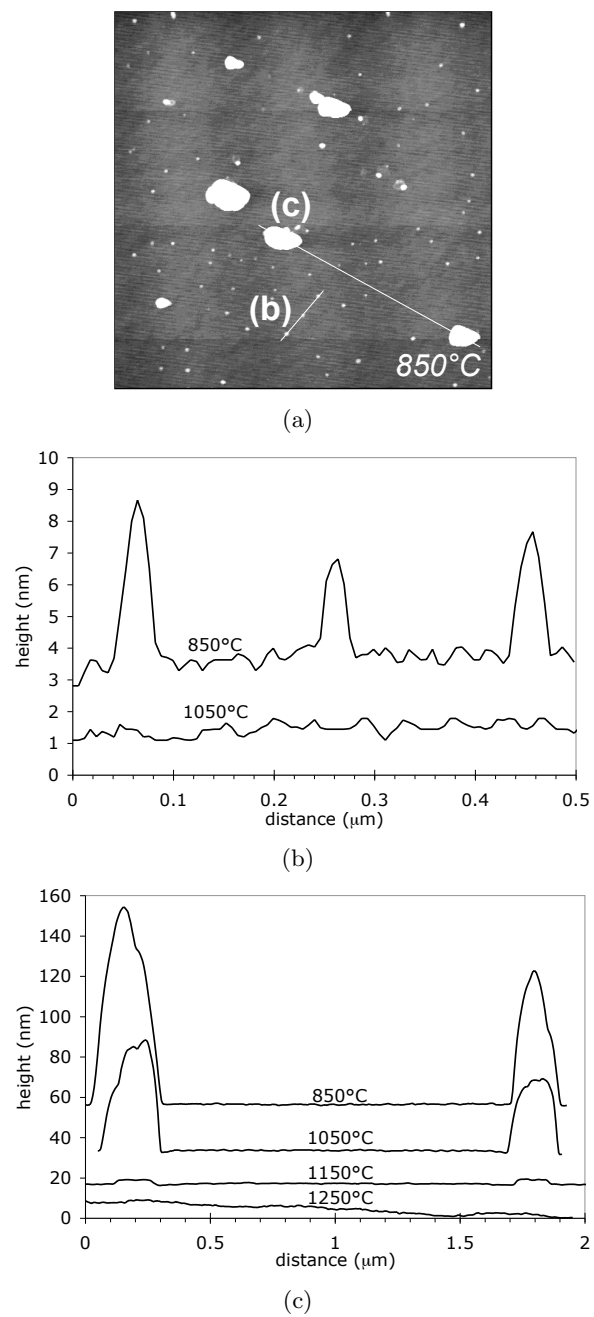


Figure 4:

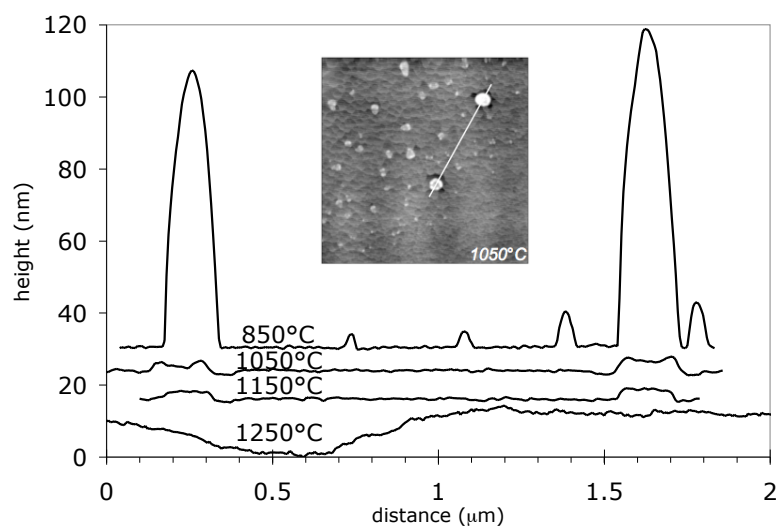


Figure 5:

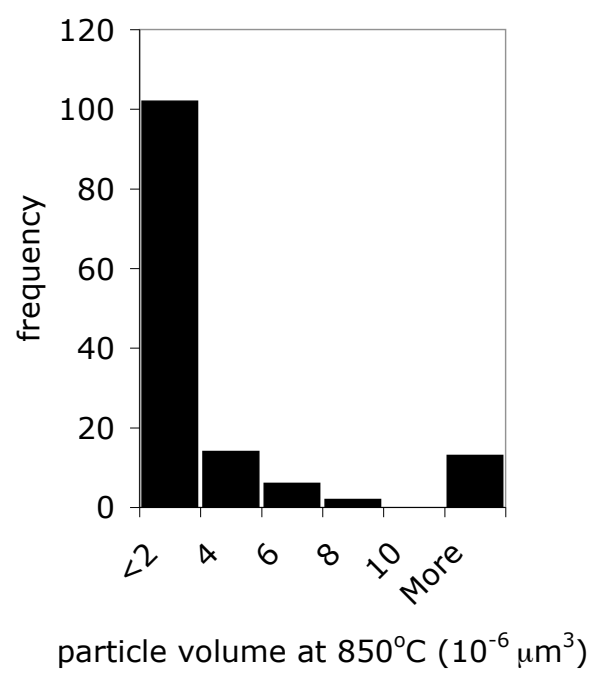


Figure 6:

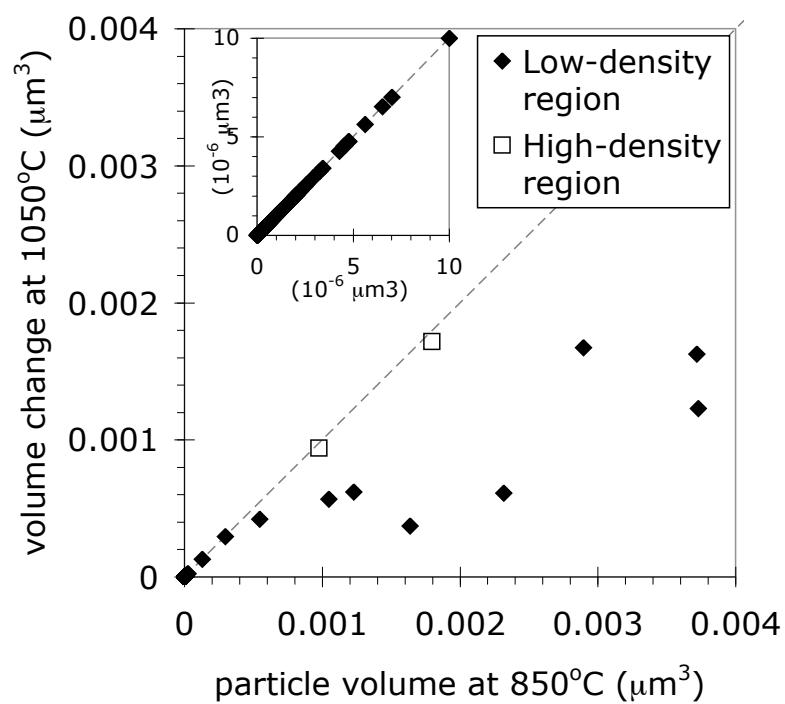


Figure 7:

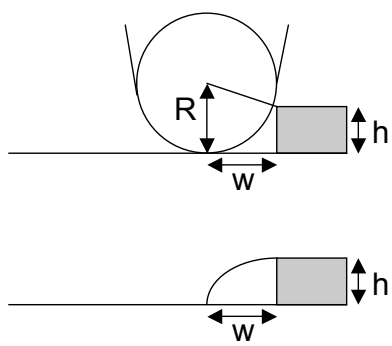


Figure 8:

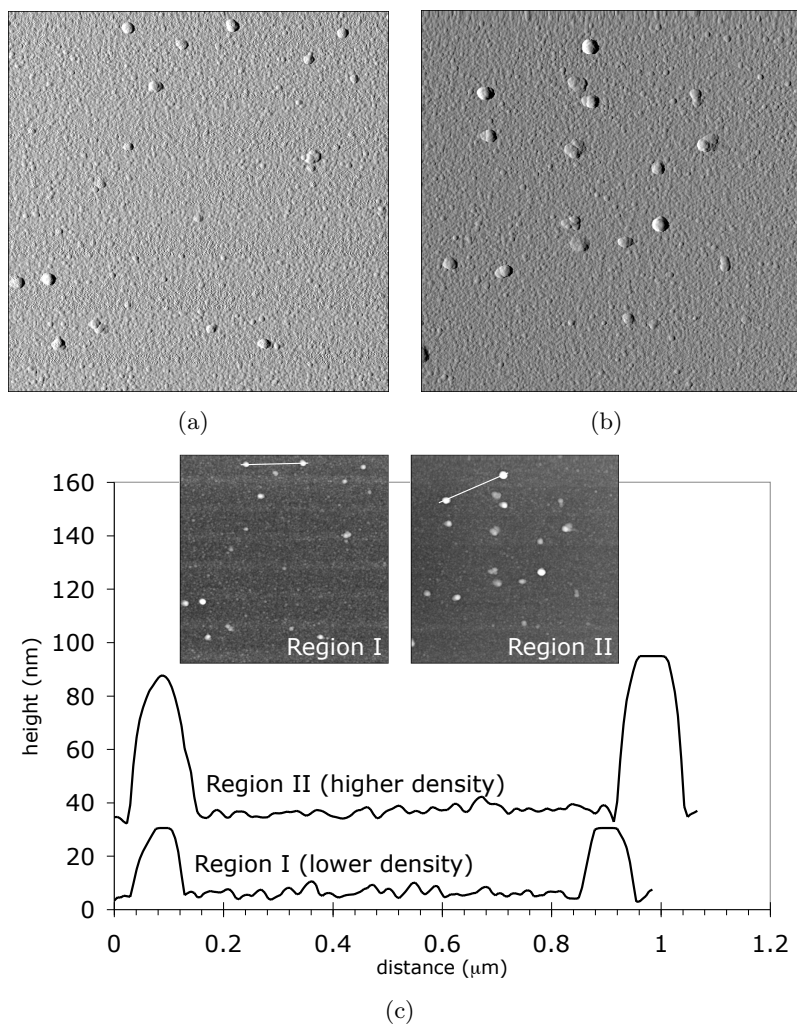


Figure 9:

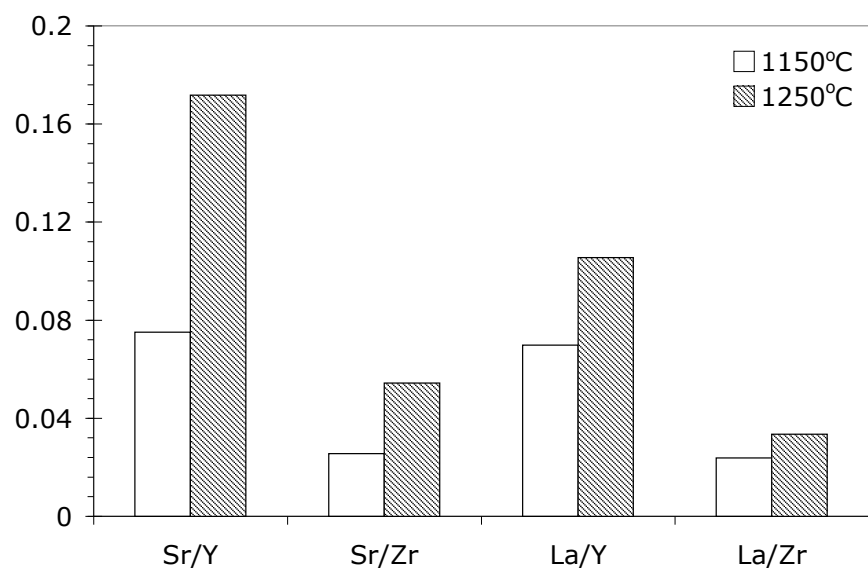


Figure 10:



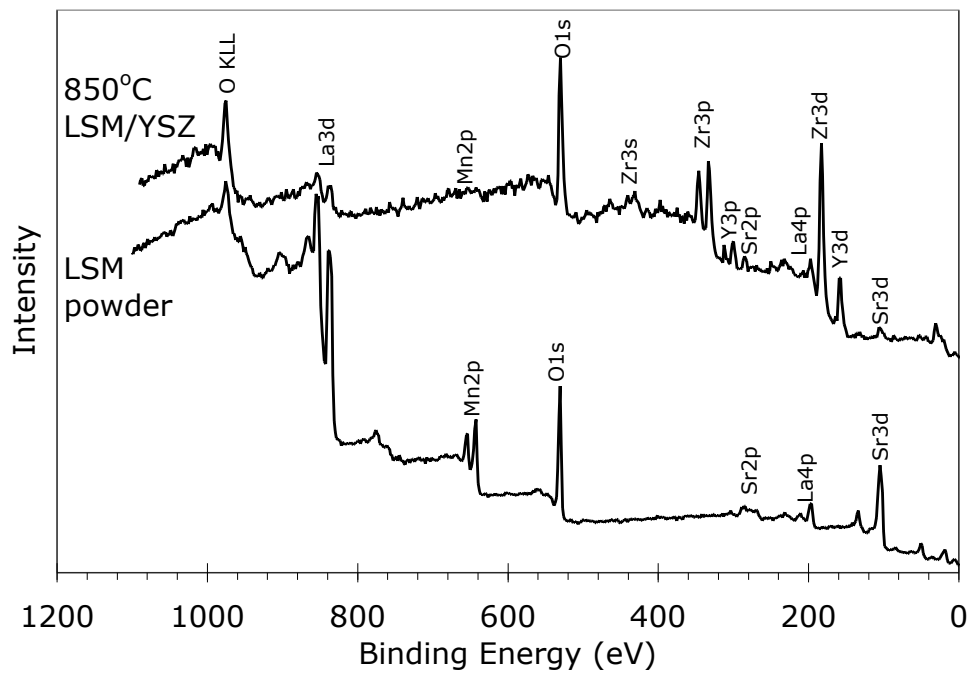


Figure 11:

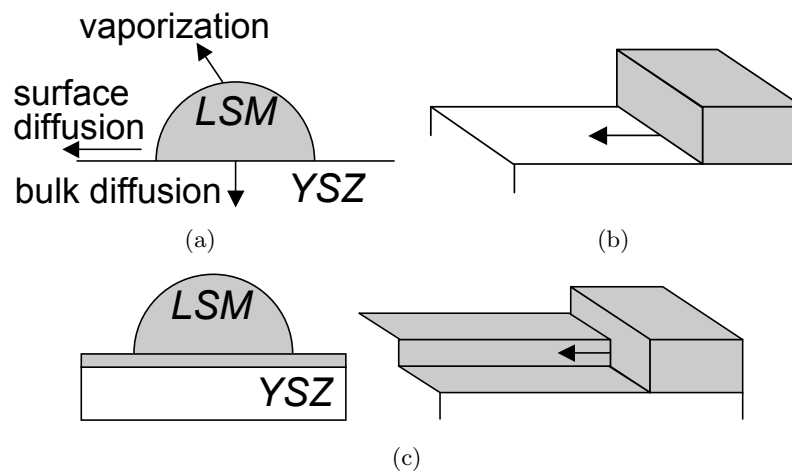


Figure 12: